Hindawi
Advances in Materials Science and Engineering
Volume 2020, Article ID 9430875, 12 pages
https://doi.org/10.1155/2020/9430875

Research Article

A Trans-Scale Young' Modulus Calculation Model of ITZ Based on Void Shape Randomness and Calcium Hydroxide Enrichment

Junqing Liu,[1] Fan Zuo,[2] and Chao Liu [1,3]

[1]*School of Science, Xi'an University of Architecture and Technology, Xi'an, Shaanxi 710055, China*
[2]*School of Civil Engineering, Xi'an University of Architecture and Technology, Xi'an, Shaanxi 710055, China*
[3]*Shaanxi Key Laborotary of Geotechnical and Underground Space Engineering, Xi'an University of Architecture and Technology, Xi'an, Shaanxi 710055, China*

Correspondence should be addressed to Chao Liu; chaoliu@xauat.edu.cn

Received 2 May 2020; Revised 28 June 2020; Accepted 30 June 2020; Published 26 August 2020

Academic Editor: Barbara Liguori

The randomness of void shape and enrichment of calcium hydroxide are significant in interfacial transition zone (ITZ) of concrete; however, current theoretical models of ITZ do not include these features. In this article, ITZ was regarded as a three-phase composite material, and the pore morphological parameters were defined according to the characteristics of microscopic pores, and the corresponding random distribution function was constructed. The calcium hydroxide enrichment factor was introduced, and a cross-scale ITZ Young's modulus calculation model was established in combination with the Mori–Tanaka method. The reliability of the proposed model in this paper was verified through comparison to experimental results in a reference.

1. Introduction

As the weak area between aggregate and bulk paste in concrete, the interfacial transition zone (ITZ) influences mechanical properties of concrete, including Young's modulus, strength, and cracking behavior significantly [1–7]. Concrete was treated as a two-phase composite composed of aggregate and bulk paste in early studies, but study on limestone aggregate concrete conducted by Nilsen and Monterio [8] revealed that the tested Young's modulus values were lower than Hashin–Shtrikman lower limit under two-phase assumption. Simeonov and Ahamd [5] observed increasing deviation between test results and Hashin–Shtrikman limit under two-phase assumption with the increasing of aggregate volume fraction.

ITZ was began to be taken into consideration [3] to solve the problem of large difference between the model-calculated results and experimental results. Analysis of Chun'an et al. [9] showed that the properties of transition zone between inclusions and the matrix influence the stress field inside the composite, which then influences damage location and failure mode consequently. Studies of Liu et al. [10, 11] revealed the impact of ITZ on long-term deformation and bond behavior of recycled concrete. Three-phase models considering ITZ were established by Lee and Park [1], Zhao and Chen [12], and Nadeau [13] et al., and reliable results were obtained. The failure mechanism of concrete under high strain rate with a three-phase model was studied by Zhou and Hao [7], and this study showed that it influences the failure mode, failure time, and tensile strength remarkably. Berger [14] held that the wall effect led to higher porosity of cement paste on aggregate surface, which created a suitable circumstance for migration of water and ions and resulted in enrichment of calcium hydroxide and ettringite on aggregate surface. Simeonov and Ahamd [5] et al. pointed out the unsteadiness of ITZ properties along direction perpendicular to aggregate surface.

Experimental and theoretical methods were used to study many aspects of ITZ. The ITZ nanoindentation tests of gravel concrete and limestone concrete by Mondal [15] revealed that Young's modulus of ITZ has a gradient of change in the direction perpendicular to the surface of the aggregate, and the test results at different measuring points have large dispersion. Other experimental results on ITZ in self-compacting concrete [16], rock-filled concrete [17],

nanosilica modified concrete [18], and sugarcane industrial ash modified concrete [19] also showed similar characteristics. X-ray diffraction (XRD) was used by Hagis [20] to study the microstructure of cement hydration products, and the result showed that the microstructure and pore characteristics of calcium hydroxide, ettringite, and hydrated calcium silicate gels are significantly different. Mercury intrusion test was used by Liu et al. [21] to study the influence of porosity on water and ion migration in ITZ. Scanning electron microscopy (SEM) was used by Barnes et al. [22] to study the evolution of the microstructure of the glass-cement mortar interface transition zone. The result showed that calcium hydroxide enrichment contributes greatly to the formation of ITZ high porosity. Sun et al. investigated the effects of aggregate surface by coating slag and silica fume on the ITZ microstructure [23] and studied the transport behavior of sulfate ions in concrete-containing ITZ [24]. Their studies showed that the ettringite formation inside the concrete pores influences the elastic deformation behavior of concrete significantly [25].

The most common theoretical method for calculating ITZ Young's modulus is the discount coefficient method: a discount coefficient is imposed on Young's modulus of cement paste, and the discounted result is used as the corresponding parameter of ITZ [7, 12, 13]. Luts and Zimmerman [26] believed that ITZ Young's modulus is related to aggregate size, distance from aggregate surface, and modulus of bulk paste. They assumed that ITZ Young's modulus can be calculated by a power-law function. Nadeau [27] proposed a theoretical calculation method of ITZ Young's modulus, which comprehensively considered the influence of water-cement ratio, aggregate volume fraction, cement specific gravity, ITZ thickness, and other factors. However, so far, there is still no ITZ Young's modulus calculation model that can essentially consider the void shape randomness and calcium hydroxide enrichment caused by the characteristics of ITZ components and reflect the variation along direction perpendicular to aggregate surface and the discreteness among results of different measured points.

A trans-scale calculation model of ITZ Young's modulus is proposed in this paper. In this model, ITZ is adopted to three-phase composite, void shape parameter and calcium hydroxide enrichment parameter are defined, and then ITZ Young's modulus could be calculated with the Mori–Tanaka method. The calculation model comprehensively considers the randomness of void shape and the degree of calcium hydroxide enrichment caused by the characteristics of ITZ components. It has the advantages of covering the upper and lower limits of Young's modulus, reflecting the gradient of Young's modulus change and small calculation. By comparison with the test results in a reference, the validity of the calculation model is verified. This model could calculate ITZ Young's modulus reliably and quickly and provides a theoretical basis for the calculation of concrete mechanical properties.

2. Three-Phase Composite Model of ITZ

ITZ is a thin layer caused by the wall effect occurred between the aggregate and the bulk paste [14]. The resistance of aggregate on water permeation and cement accumulation lead to higher water-cement ratio and porosity compared with cement paste; meanwhile, the enrichment of calcium hydroxide crystal is rather notable. Thus, ITZ could be considered as a layer of near-field cement paste with high water-cement ratio, high porosity, and enriched calcium hydroxide crystal, and the water-cement ratio, porosity, and enrichment of calcium hydroxide reduce with the distance to the aggregate increasing.

The major components of ITZ remain consistent with the cement paste [15], which include hydrated calcium silicate gel (CSH, which contains low-density CSH and high-density CSH, contracts to LD-CSH and HD-CSH, respectively), calcium hydroxide (CH), and ettringite. However, the volume fractions of components in ITZ are different with those in cement paste, considering the enrichment of CH. The microcrystal shape and pore features of ITZ components differ largely through electron microscopy [20, 28, 29], as is shown in Figure 1.

The macromechanical properties of cement paste in far or near-field are closely related to micromechanical properties and volume fraction of components, while those of components are closely related to corresponding microstructures and pore features. The micro- and macrofeatures of components should be taken into consideration in the calculation of ITZ mechanical properties, and a trans-scale model could be established.

Cement paste was treated as a four-phase composite in previous studies [30]: micropores, LD-CSH, HD-CSH, and ettringite. However, it is necessary to take the differences between ITZ and cement paste into account: pores stem from the special crystal structures of CH and ettringite rather than air holes; the volume fraction of micropores is not equal to the absolute porosity of bulk paste, which leads to the difference on mechanical properties and volume fractions between ITZ components and bulk paste components.

In addition, phases of ITZ grow and stagger throughout the hydration of cement. Influence of local pores leads to local randomness of property in each phase, following the local randomness of phases leads to general randomness of composite. More attention on local randomness led by pores is necessary in trans-scale modeling.

This paper presents a trans-scale ITZ model used for Young's modulus calculation, which takes the randomness of pores and phases into account. This model adopted a three-phase model, which consists of LD-CSH, HD-CSH, and CH, voids with shape randomness distributed in three phases. The assumption of continuously uniform media was applied into cement paste, and the relative porosity of ITZ to cement paste was set as the porosity of phases; methods of composite materials were used in mechanical property calculation of phases.

The following 3 steps were needed in trans-scale modeling:

(1) In the microscale level

1st step: it was assumed that all the pores distribute in the phases continuously. Each phase was regarded as an accumulation of representative volume element (RVE) with an independent void in

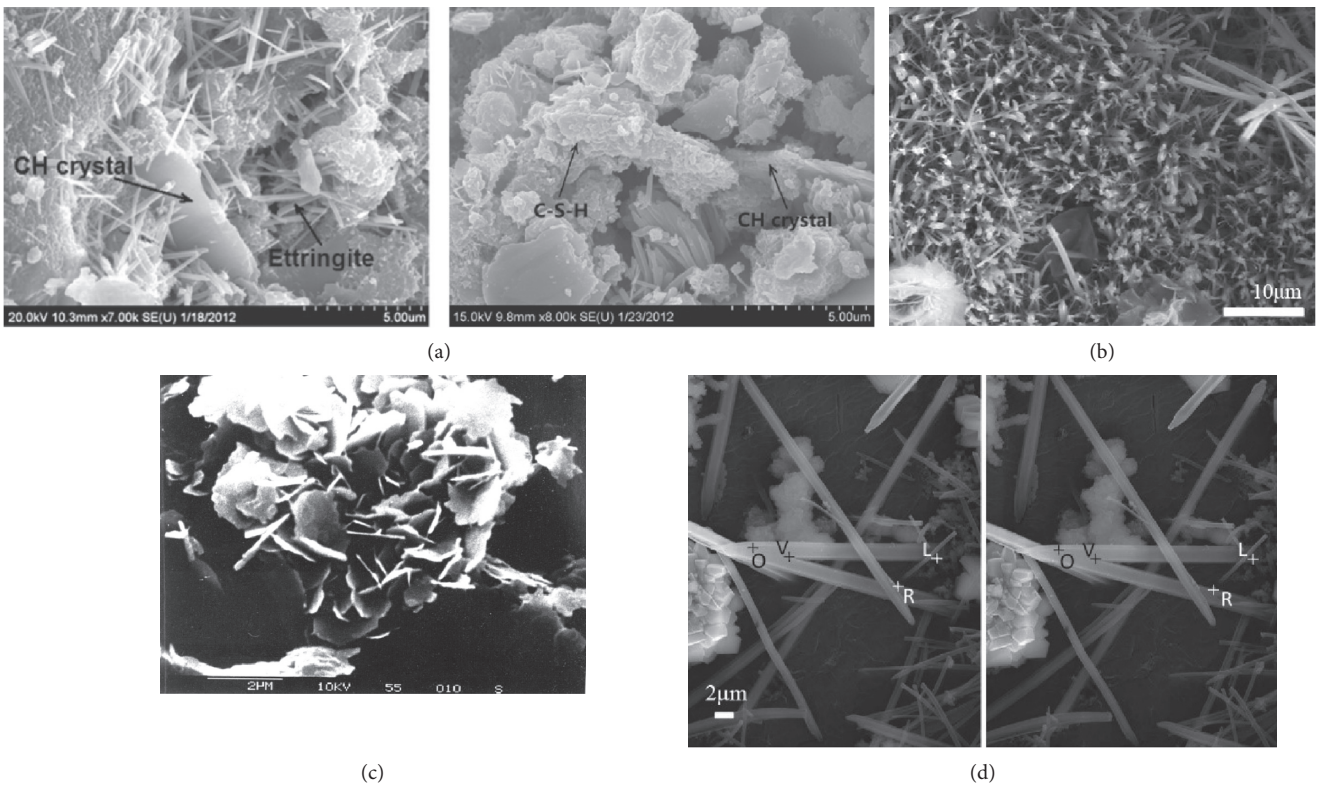

Figure 1: Micromorphology of components in ITZ [20, 28, 29]. (a) Micromorphology of ITZ [28]. (b) Micromorphology of CSH [20]. (c) Micromorphology of CH [29]. (d) Micromorphology of ettringite [20].

the center, and the porosity of each RVE was consistent with others. The shape of voids corresponded with some distribution, the shape parameter was defined, and corresponding distribution functions were constructed so that the features of void shape and distribution were described. The method of composite material was used to gain the mechanical properties of each RVE. 2nd step: each RVE was treated as a part of a certain phase, and thus, each phase could be regarded as a combination of n-RVEs, that is, an n-phase composite. The mechanical properties of each phase were obtained through the composite material method.

(2) In the macroscale level

3rd step: ITZ was considered as a 3-phase composite consisted of LD-CSH, HD-CSH, and CH, and the macro Young's modulus of ITZ was obtained.

The modeling of the trans-scale model is shown in Figure 2.

3. Trans-Scale Model of Young's Modulus in ITZ

3.1. Equivalence of Microvoid Shape and the Shape Parameter. An accurate description on void features of phases in ITZ is necessary for calculation. Voids could be treated as special inclusions with zero modulus. The inclusion with a shape of rotating ellipsoid, in which 2 in 3 axes are of equal length, is a kind of inclusions with excellent universal adaptability. Various kinds of inclusions, such as spherical, ellipsoidal, penny-shaped, and cylindrical inclusions [31], are the generalization of rotating ellipsoidal inclusion. Considering the complexity of void shape in ITZ, this paper assumed that all the voids in ITZ phases are in the shape of rotating ellipsoid.

The phases in cement paste appear significantly different according to the SEM images: the crystal polymer of CSH is dense and uniform, and that of CH appears like a peony, while that of ettringite is needle-like, which is easy to form an extremely loose structure. Based on the shape and shape randomness of voids in phases, it is a reasonable assumption that the RVEs corresponding to CSH contain mainly spherical voids, CH contains mainly rotating ellipsoidal voids, and ettringite are treated as a pure void without any matrix. Considering the staggering of all the phases, it is acceptable to put the "ettringite voids" into other RVEs as part of porosity instead of an independent phase, as is shown in Figure 3.

A typical RVE was set to be a cube with 2L in side length, containing a rotating ellipsoidal void with a_1, a_2, and a_3 in 3 axis length, respectively, where $a_2 = a_3$. The void shape parameter α was defined as

$$\alpha = \frac{a_1}{a_3}. \tag{1}$$

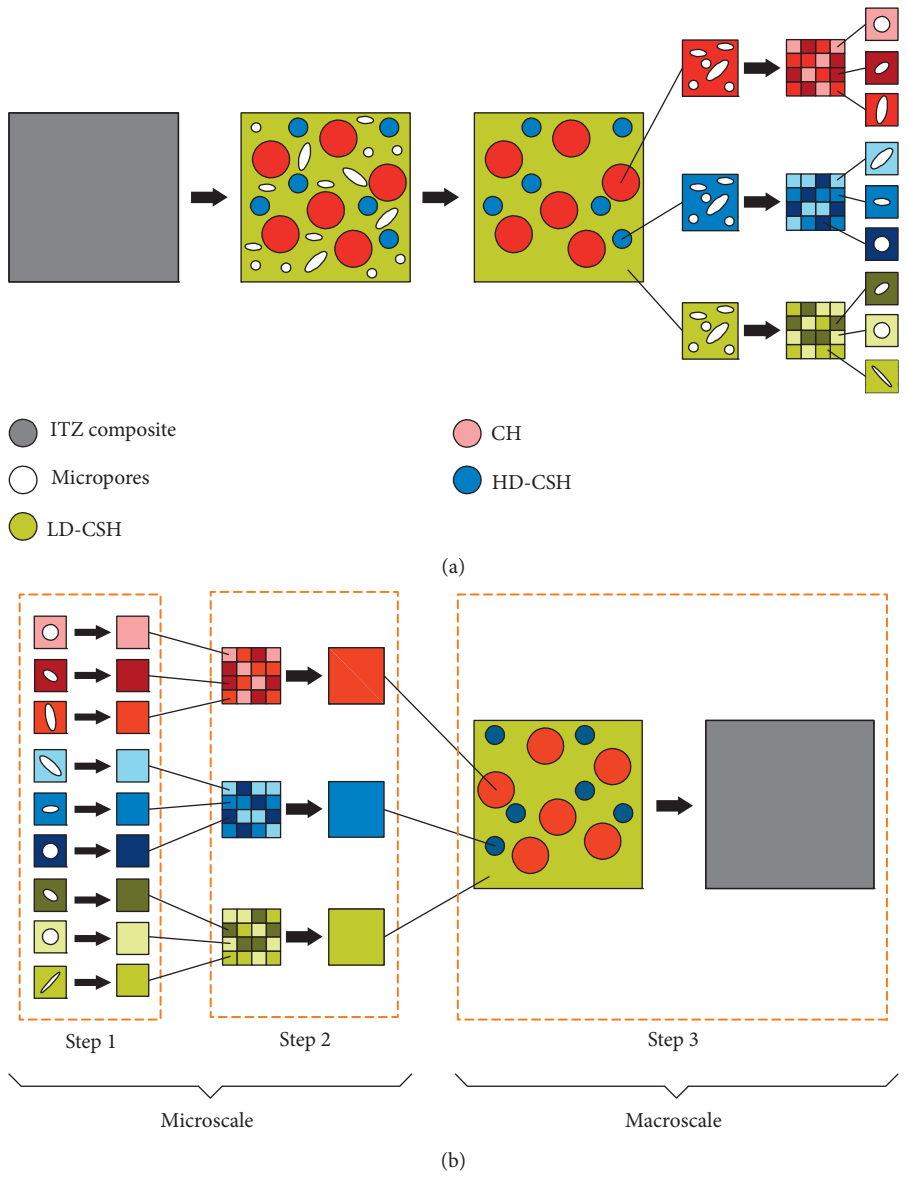

Figure 2: Trans-scale modeling. (a) Trans-scale analyzing procedure. (b) Trans-scale modeling procedure.

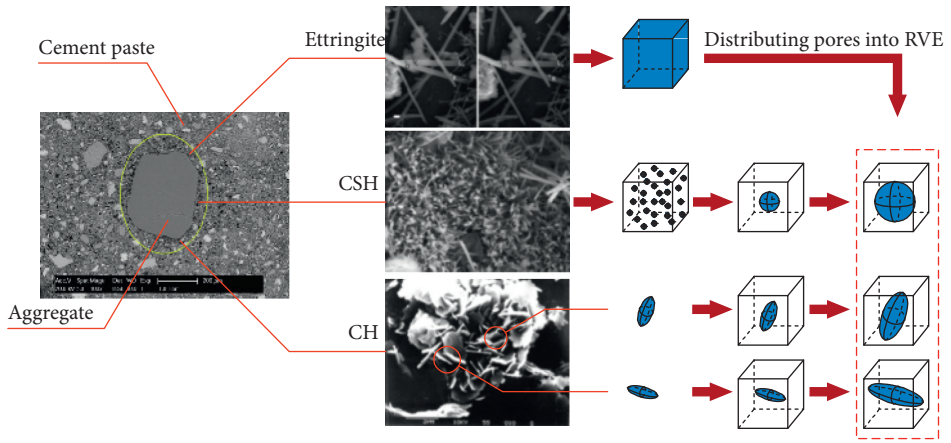

Figure 3: Equivalence of pores in phases of cement paste.

The rotating ellipsoidal void could be classified to 3 types according to the value of α: flat rotating ellipsoidal void, spherical void, and prolate rotating ellipsoidal void, as is shown in Figure 4. Eshelby tensors [31] of the voided RVE corresponding to different α are shown in Appendix A.

Based on the fact that $0 < a_1, a_2, a_3 \le L$ and $a_2 = a_3$, $\alpha = a_1/a_3$, it follows that

$$f_0 = \frac{4/3\pi a_1 a_2 a_3}{(2L)^3} = \frac{\pi}{6}\alpha\left(\frac{a_3}{L}\right)^3 = \frac{\pi}{6}\alpha^{-2}\left(\frac{a_1}{L}\right)^3, \quad (2)$$

and by reforming equation (2), we can get

$$\alpha = \frac{6f_0}{\pi(a_3/L)^3} = \left(\frac{6f_0}{\pi(a_1/L)^3}\right)^{-1/2}, \quad 0 < a_1 < L, 0 < a_3 < L. \quad (3)$$

The domain of α could be concluded as

$$\left(\frac{\pi}{6f_0}\right)^{-1} < \alpha < \left(\frac{\pi}{6f_0}\right)^{1/2}. \quad (4)$$

Denote

$$\alpha_{cr} = \left(\frac{\pi}{6f_0}\right)^{1/2}, \quad (5)$$

and then the domain of α was reformed to

$$\alpha_{cr}^{-2} < \alpha < \alpha_{cr}. \quad (6a)$$

For the purpose of a more tractable parameter, denote $\gamma = \alpha_{cr}^{1/2}\alpha$, and then equation (6a) could be reformed further as

$$\alpha_{cr}^{-3/2} < \gamma < \alpha_{cr}^{3/2}. \quad (6b)$$

The void is spherical when $\alpha = 1, \gamma = \alpha_{cr}^{1/2}$, flat rotating ellipsoidal when $\alpha > 1, \gamma > \alpha_{cr}^{1/2}$, and prolate rotating ellipsoidal when $\alpha < 1, \gamma < \alpha_{cr}^{1/2}$. γ and α are equivalent in the following analysis.

3.2. Distribution Functions of Shape Parameter. The differences among microstructures of each phase in cement paste led to the differences among corresponding void shapes. For the voids in the RVE corresponding to CSH, the most probable values of shape parameters were $\mathrm{Mo}(\alpha) = 1, \mathrm{Mo}(\gamma) = \alpha_{cr}^{1/2}$, while those to CH were $\mathrm{Mo}(\alpha) > 1$, $\mathrm{Mo}(\gamma) > \alpha_{cr}^{1/2}$, or $\mathrm{Mo}(\alpha) < 1, \mathrm{Mo}(\gamma) < \alpha_{cr}^{1/2}$. In accordance with the most probable values, the possible probability density functions of α and γ are shown in Figure 5. Five kinds of distribution functions were constructed consequently to describe the distribution of α and γ.

3.2.1. Distribution of Shape Parameter for $\mathrm{Mo}(\alpha) = 1$. In this case, $\mathrm{Mo}(\alpha) = 1$, $P(\alpha > 1) = P(\alpha < 1) = 1/2$; that is, $\mathrm{Mo}(\gamma) = \alpha_{cr}^{1/2}$, $P(\gamma > \alpha_{cr}^{1/2}) = P(\gamma < \alpha_{cr}^{1/2}) = 1/2$. A reasonable assumption is that γ follows the lognormal distribution [32]:

$$\gamma \sim \mathrm{LN}\left(\ln \alpha_{cr}^{1/2}, \sigma\right), \quad (7)$$

and the distribution function is

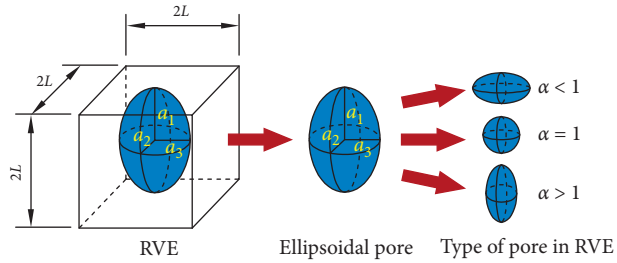

Figure 4: Voided RVE.

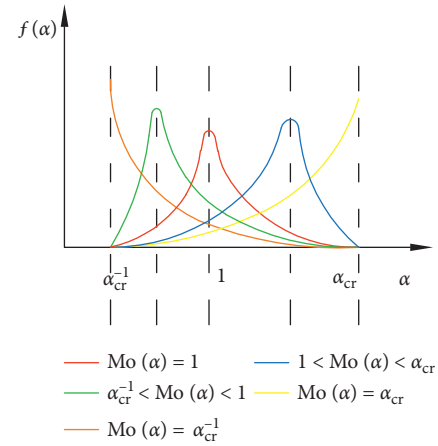

Figure 5: Possible probability density function curves of α.

$$F(\gamma) = \Phi\left(\frac{\ln\gamma - \ln\alpha_{cr}^{1/2}}{\sigma}\right), \quad \alpha_{cr}^{-3/2} < \gamma < \alpha_{cr}^{3/2}. \quad (8)$$

3.2.2. Distribution of Shape Parameter for $\mathrm{Mo}(\alpha) < 1$. In this case, $\alpha_{cr}^{-2} \le \mathrm{Mo}(\alpha) < 1$, $\alpha_{cr}^{-3/2} \le Mo(\gamma) < \alpha_{cr}^{1/2}$. The lognormal-Pareto combined distribution was constructed [33] to describe the distribution of shape parameters, denoted as $\gamma \sim \mathrm{LNP}(\beta, \theta, \sigma)$, and the distribution function is

$$F(\gamma) = \begin{cases} (1-\omega)\dfrac{F_{\mathrm{LN}}(\gamma)}{F_{\mathrm{LN}}(\theta)}, & \alpha_{cr}^{-3/2} \le \gamma < \theta, \\ 1 - \omega\dfrac{1 - F_P(\gamma)}{1 - F_P(\theta)}, & \theta \le \gamma < \alpha_{cr}^{3/2}, \end{cases} \quad (9)$$

where

$$F_{\mathrm{LN}}(\gamma) = \Phi\left(\frac{\ln\gamma - \mu}{\sigma}\right), \quad -\infty < \gamma < +\infty, \quad (10a)$$

$$F_P(\gamma) = 1 - \theta^{\beta}\gamma^{-\beta}, \quad 0 < \theta \le \gamma, \quad (10b)$$

$$\mu = \ln\theta - \beta\sigma^2, \quad (11a)$$

$$\omega = \frac{1}{1 + \sqrt{2\pi}\beta\sigma\Phi(\beta\sigma)\exp\left[0.5(\beta\sigma)^2\right]}. \quad (11b)$$

In the extreme case, $\mathrm{Mo}(\alpha) = \alpha_{cr}^{-2}, \mathrm{Mo}(\gamma) = \alpha_{cr}^{-3/2}$, and $\omega = 1$. γ follows Pareto distribution, denoted as $\gamma \sim P(\beta, \theta)$. The distribution function is

$$F(\gamma) = 1 - \theta^{\beta}\gamma^{-\beta}, \quad \theta = \alpha_{cr}^{-3/2}, \alpha_{cr}^{-3/2} \le \gamma \le \alpha_{cr}^{3/2}. \tag{12}$$

3.2.3. Distribution of Shape Parameter for $Mo(\alpha) > 1$. In this case, $1 < \mathrm{Mo}(\alpha) \le \alpha_{cr}, \alpha_{cr}^{1/2} < \mathrm{Mo}(\gamma) \le \alpha_{cr}^{3/2}$. The domain of γ is completely conjugated with that in Section 3.2.2. Therefore, transforming γ to a conjugated parameter u and then the conjugated distribution function could be reconstructed. The method is as follows.

Denote u as the conjugated parameter of γ, $G_P(u), G_{\mathrm{LN}}(u)$ as the conjugated distribution function of $F_P(u), F_{\mathrm{LN}}(u)$. Obviously,

$$u = t(\gamma) = \frac{1}{\gamma}, \quad \alpha_{cr}^{-3/2} \le u \le \alpha_{cr}^{3/2}. \tag{13}$$

The monotonicity of u and γ is in contrary, then $F_P(u)$ and $F_{\mathrm{LN}}(u)$ should be monotone decreasing consequently, and numerical range of which should be $(0, 1)$. Guaranteeing the monotonicity and numerical range, $G_P(u), G_{\mathrm{LN}}(u)$ could be constructed as

$$G_P(u) = 1 - F_P(u) = \theta^{\beta}u^{\beta}, \tag{14a}$$

$$G_{\mathrm{LN}}(u) = 1 - F_{\mathrm{LN}}(u) = \Phi\left(\frac{\ln u + \mu}{\sigma}\right). \tag{14b}$$

The reconstructed distribution is named conjugated Pareto-lognormal combined distribution, denoted as $\gamma \sim \mathrm{con\_LNP}(\beta, \theta, \sigma)$. The distribution function is

$$G(\gamma) = \begin{cases} \omega \dfrac{G_P(\gamma)}{G_P\left(\theta^{-1}\right)}, & \alpha_{cr}^{-3/2} < \gamma < \theta^{-1}, \\ 1 - (1-\omega)\dfrac{1 - G_{\mathrm{LN}}(\gamma)}{1 - G_{\mathrm{LN}}\left(\theta^{-1}\right)}, & \theta^{-1} \le \gamma < \alpha_{cr}^{3/2}. \end{cases} \tag{15}$$

The calculation of ω and μ is the same with equation (11).

In the extreme case, $\mathrm{Mo}(\alpha) = \alpha_{cr}, \mathrm{Mo}(\gamma) = \alpha_{cr}^{3/2}$and $\omega = 1$. γ follows the conjugated Pareto distribution, denoted as $\gamma \sim \mathrm{con\_}P(\beta, \theta)$, and the distribution function is

$$G(\gamma) = \frac{G_P(\gamma)}{G_P\left(\theta^{-1}\right)} = \theta^{\beta}\gamma^{\beta}, \quad \alpha_{cr}^{-3/2} < \gamma < \theta^{-1}, \theta^{-1} = \alpha_{cr}^{3/2}. \tag{16}$$

As the distribution functions are obtained, α_{cr} could be obtained with a known f_0, and other parameters in distribution functions could be calculated with a corresponding quantile.

3.3. Equivalent Modulus of RVEs Corresponding to Phases. The porosity of the ith phase was denoted as c_i, the Poisson ratio as ν_{i0}, and Young's modulus as E_{i0}. This phase is composed of n-RVEs, each RVE contains a void with a shape parameter of α, and the porosities of all the RVEs are the same c_i. Massive α values could be gain through the Monte Carlo sampling method, with a certain distribution function correspondingly.

The average mechanical properties of RVEs are worthy to be adopted in consideration of the randomness of void axis directions in the RVE accumulation. The average volume modulus κ and the average shear modulus μ of an RVE with an α valued shape parameter and random axis direction could be obtained by Mori–Tanaka method [34]:

$$\kappa(\alpha) = \frac{\kappa_{i0}}{1 + c_i p}, \qquad \mu(\alpha) = \frac{\mu_{i0}}{1 + c_i q}, \tag{17}$$

respectively, where p and q are decided by the Eshelby tensor [34].

The macroporosity, Poisson ratio, and Young's modulus of each phase would be determined in the next part then the macro Young's modulus of ITZ, consequently.

3.4. Related Parameters of Cement Paste. As the distance between the cement paste and the aggregate surface increases, the influence of the side wall effect gradually weakens, the local water-cement ratio decreases, the porosity decreases, the degree of calcium hydroxide enrichment weakens, and the porosity and volume fraction of the constituent phases decrease. The porosity and volume fraction of the constituent phases also change.

ITZ is a layer of high-porosity cement paste. Taking the porosity of the cement paste and the compositional phase volume fraction as a reference, the local porosity of ITZ was determined based on the local water-cement ratio, and the relative porosity of ITZ was obtained. The degree of calcium hydroxide enrichment of ITZ was determined, based on which the volume fraction of the cement mortar composition phase was adjusted, and the volume fractions of the ITZ composition phases were obtained. After ITZ's relative porosity and composition phase volume fraction were obtained, the ITZ modulus calculation can be performed.

The volume fractions of components in cement paste were denoted as $c_{\mathrm{HD-CSH}}^0$ and $c_{\mathrm{LD-CSH}}^0$ and CH as c_{CH}^0. The relative volume fractions among LD-CSH, HD-CSH, and CH are almost unchanged under the water-cement ratio of 0.5 and 0.65, respectively [15]. Without test result under higher water-cement ratio, it is reasonable to assume that, for the cement paste with a water-cement ratio $w_0 \ge 0.5$, the relative volume fractions of the 3 phases keep as the average value of that under 0.5 and 0.65 water-cement ratio, as is shown in Table 1.

Young's modulus of phases in cement paste is shown in Table 2, in which that of micropores(MC) was set to be zero in this paper. The Poisson ratios of all the phases were set to be 0.2.

The absolute porosity of cement paste, φ bulkabs, was set to be 30.7% when $w_0 = 0.5$ [35].

It is worth noting that Young's modulus of phases in cement paste provided by [15] is affected by the micropores in the phases themselves, while the micropores are contained in the absolute porosity of cement paste. There would be a higher estimation on actual porosity if the test results in [13] are adopted directly. To avoid this problem, it is supposed to treat the volume fraction of micropores, c^0_{mc}, as the relative porosity of cement paste, $\varphi^{\mathrm{re}}_{\mathrm{bulk}}$. Then, the porosity of phases could be calculated as follows:

$$\varphi^{\mathrm{abs}}_{\mathrm{phase}} = \frac{\varphi^{\mathrm{abs}}_{\mathrm{bulk}} - \varphi^{\mathrm{re}}_{\mathrm{bulk}}}{1 - \varphi^{\mathrm{re}}_{\mathrm{bulk}}} \cdot 100\%, \tag{18}$$

in which $\varphi^{\mathrm{re}}_{\mathrm{bulk}} = 10\%$ and $\varphi^{\mathrm{abs}}_{\mathrm{bulk}} = 30.7\%$ when $w_0 = 0.5$ [35], and thus, $\varphi^{\mathrm{abs}}_{\mathrm{phase}} = 23\%$.

3.5. Macro Young's Modulus of ITZ considering the Enrichment of CH

3.5.1. Local Water-Cement Ratio and Relative Porosity of ITZ. As is discussed in 3.4, in accordance with the influence of bulk paste porosity on tested modulus of cement paste phases, it is necessary to adopt the relative porosity of ITZ to bulk paste in calculation of ITZ modulus, to avoid an over estimation on porosity.

The local water-cement ratio, w, could be calculated as [27]

$$w(d) = \frac{1 - \alpha_c(d)}{G_c \alpha_c(d)}, \tag{19}$$

where

$$\alpha_c(d) = \begin{cases} \overline{\alpha}_c \left[1 + a_c \left(\frac{d-\delta}{\delta}\right)^2\right], & 0 < d \le \delta, \\ \overline{\alpha}_c, & d \ge \delta, \end{cases} \tag{20a}$$

$$\overline{\alpha}_c = \frac{10(1 - c_a)}{(1 + w_0)\left\{a_c c_a \delta / r_a \left[(\delta/r_a)^2 + 5\delta/r_a + 10\right] + 10(1 - c_a)\right\}}, \tag{20b}$$

in which $G_c = 3.15, a_c = -0.4959$, δ is the thickness of ITZ, r_a is the radius of aggregate, c_a is the volume fraction of aggregate, and w_0 is the water-cement ratio of bulk paste, as is shown in Figure 6.

The relation between the distance from aggregate surface and porosity is [35]

$$\varphi^{\mathrm{abs}}(d) = \begin{cases} \varphi^{\mathrm{abs}}_{\mathrm{ITZ}} - \left(\varphi^{\mathrm{abs}}_{\mathrm{ITZ}} - \varphi^{\mathrm{abs}}_{\mathrm{bulk}}\right)\left(\frac{d}{\delta}\right)^{\beta}, & 0 < d \le \delta, \\ \varphi^{\mathrm{abs}}_{\mathrm{bulk}}, & \delta \le d, \end{cases} \tag{21}$$

where $\varphi^{\mathrm{abs}}_{\mathrm{ITZ}}$ is the absolute porosity when $d = 0$. $\varphi^{\mathrm{abs}}_{\mathrm{ITZ}} = 78.9\%, \beta = 0.49$, and $\varphi^{\mathrm{abs}}_{\mathrm{bulk}} = 30.7\%$ [35] when $w_0 = 0.5$.

Table 1: Relative volume fraction of phases in cement paste when $w_0 \ge 0.5$ [15].

$c^0_{\mathrm{LD-CSH}}$	$c^0_{\mathrm{HD-CSH}}$	c^0_{CH}
68.5%	23.4%	8.1%

Table 2: Young's modulus of phases in cement paste [15].

Phases	MC	LD-CSH	HD-CSH	CH
Young's modulus (GPa)	0	16.5	25	33

The absolute porosity of cement paste, $\varphi^{\mathrm{abs}}_{\mathrm{bulk}}$, was set to be 30.7% when $w_0 = 0.5$ [35].

With a determined $\varphi^{\mathrm{abs}}(d)$, the relative porosity, $\varphi^{\mathrm{re}}(d)$, could be obtained as follows:

$$\varphi^{\mathrm{re}}(d) = \frac{\varphi^{\mathrm{abs}}(d) - \varphi^{\mathrm{abs}}_{\mathrm{phase}}}{1 - \varphi^{\mathrm{abs}}_{\mathrm{phase}}}. \tag{22}$$

3.5.2. Enrichment Parameter of CH. The enrichment degree of CH is proportional to the local relative porosity. An enrichment parameter, η, was introduced to estimate the enrichment degree of CH as follows:

$$\eta = \eta\left(\varphi^{\mathrm{re}}\right). \tag{23}$$

The form of equation (23) depends on test results, which were determined in the 4th part of this paper. In accordance with an assumption of a constant volume fraction ratio between LD-CSH and HD-CSH, the volume fraction ratio of ITZ with consideration of CH enrichment could be obtained as follows:

$$c_{\mathrm{CH}} = \eta c^0_{\mathrm{CH}}, \tag{24a}$$

$$c_{\mathrm{LD-CSH}} = \frac{1 - \eta c^0_{\mathrm{CH}}}{c^0_{\mathrm{LD-CSH}} + c^0_{\mathrm{HD-CSH}}} c^0_{\mathrm{LD-CSH}}, \tag{24b}$$

$$c_{\mathrm{HD-CSH}} = \frac{1 - \eta c^0_{\mathrm{CH}}}{c^0_{\mathrm{LD-CSH}} + c^0_{\mathrm{HD-CSH}}} c^0_{\mathrm{HD-CSH}}. \tag{24c}$$

3.5.3. Macro Young's Modulus of ITZ. The volume and shear modulus of isotropic multiphase composite could be obtained by the Mori–Tanaka method [36]:

$$\frac{\kappa}{\kappa_0} = 1 + \frac{a}{1 - \alpha_0 a}, \qquad \frac{\mu}{\mu_0} = 1 + \frac{b}{1 - \beta_0 b}, \tag{25}$$

where

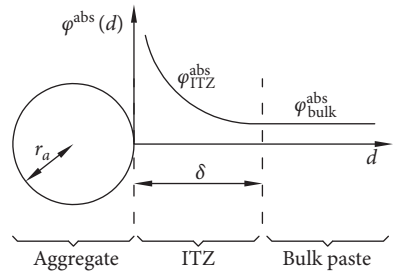

Figure 6: Absolute porosity.

$$\alpha_0 = \frac{3\kappa_0}{3\kappa_0 + 4\mu_0}, \qquad \beta_0 = \frac{6}{5}\frac{\kappa_0 + 2\mu_0}{3\kappa_0 + 4\mu_0}, \tag{26a}$$

$$a = \sum_r \frac{c_r(\kappa_r - \kappa_0)}{\alpha_0(\kappa_r - \kappa_0) + \kappa_0}, \qquad b = \sum_r \frac{c_r(\mu_r - \mu_0)}{\beta_0(\mu_r - \mu_0) + \mu_0}. \tag{26b}$$

The subscript 0 represents the bulk matrix, r is the rth phase, and c_r is the volume fraction ratio of rth phase.

4. Result and Verification

Nanoindentation tests on gravel-cement ITZ [13] were chosen for verification. Samples were made using Type I Portland cement, river sand, and gravel. Water-cement ratio was fixed at 0.5, river sand in the size of 1.18 mm to 2.36 mm, and gravels with an approximate size of 5 mm were used. All the samples were designed to be 1 inch × 1 inch × 0.5 inch, with a single gravel in the center, and cured under water at 25°C.

Seven groups of test results located at 2.5 μm to 27.5 μm from the aggregate surface were provided, 2 of which were used for parameter fitting, and the thickness of ITZ, δ, was determined to be 20 μm. With these data, according to least square principle, the form of enrichment parameter η was determined as follows:

$$\eta(\varphi^{re}) = P_1 \cdot \exp(P_2 \cdot \varphi^{re}) + Q_1 \cdot \exp(Q_2 \cdot \varphi^{re}), \tag{27}$$

and fitted parameters in which are shown in Table 3.

Considering the randomness of void shape, the calculation results were not equal to test results directly, so it is reasonable to adopt all the test results for verification. The calculated local water-cement ratio w and local porosity φ^{abs} and φ^{re} are shown in Table 4, and the parameters in distribution are shown in Appendix B.

Assumed the void shape of CH follows LN, P, con_P, PLN, and con_PLN distribution, respectively, 5 curves of ITZ Young's modulus along the distance from aggregate surface were obtained, and comparisons with test results were executed, as is shown in Figures 7 and 8.

Table 3: Parameter values in equation (27).

P_1	P_2	Q_1	Q_2
8.0	2.6	6.4	−391.3

Table 4: Local water-cement ratio and local porosity of ITZ.

d (μm)	w	φ^{abs} (%)	φ^{re} (%)
2.5	1.00	61.50	50.00
7.5	0.70	49.09	33.89
12.5	0.56	40.62	22.88
17.5	0.51	33.75	13.96
22.5	0.50	30.70	10.00
27.5	0.50	30.70	10.00

Among the tested points within ITZ ($0\,\mu m < d < 20\,\mu m$), the nearer located to the surface of aggregate, the more significant discreteness of the test results, and the lager difference among all the calculated results under different distributions. Based on the analysis in Part 3, the local porosity increases with the distance from the surface of aggregate decreases. The calculated results showed that high porosity has a greater influence on Young's modulus of ITZ than low porosity, which was proved by the discreteness of test results.

Among the tested points within ITZ ($0\,\mu m < d < 20\,\mu m$), the further located to the surface of aggregate, the lower porosity of ITZ, and the smaller difference among all the calculated results under different distributions. This phenomenon showed that the low porosity has a lesser influence on Young's modulus of ITZ, and which keeps consistent with the discreteness of test results.

One possible reason for the large discreteness of test results within bulk paste ($d > 20\,\mu m$) is the thickness of ITZ was set 20 μm, but the actual thickness of ITZ among the tested points varied. For the 2nd and 4th group of test results, the peak value of Young's modulus appeared at $d = 22.5\,\mu m$, which indicated a lager thickness of ITZ than 22.5 μm; similarly, the 6th group of test results indicated 27.5 μm. Another possible reason is the randomness of Young's modulus in bulk paste, which results in the difference of corresponding ITZ Young's modulus. The deviation between test and calculated results would significantly decrease when ignoring the 2nd, 4th, and 6th group.

The calculated results were suitable for the estimation on upper limit of Young's modulus when the void in CH was assumed to follow P or PLN distribution, the lower limit

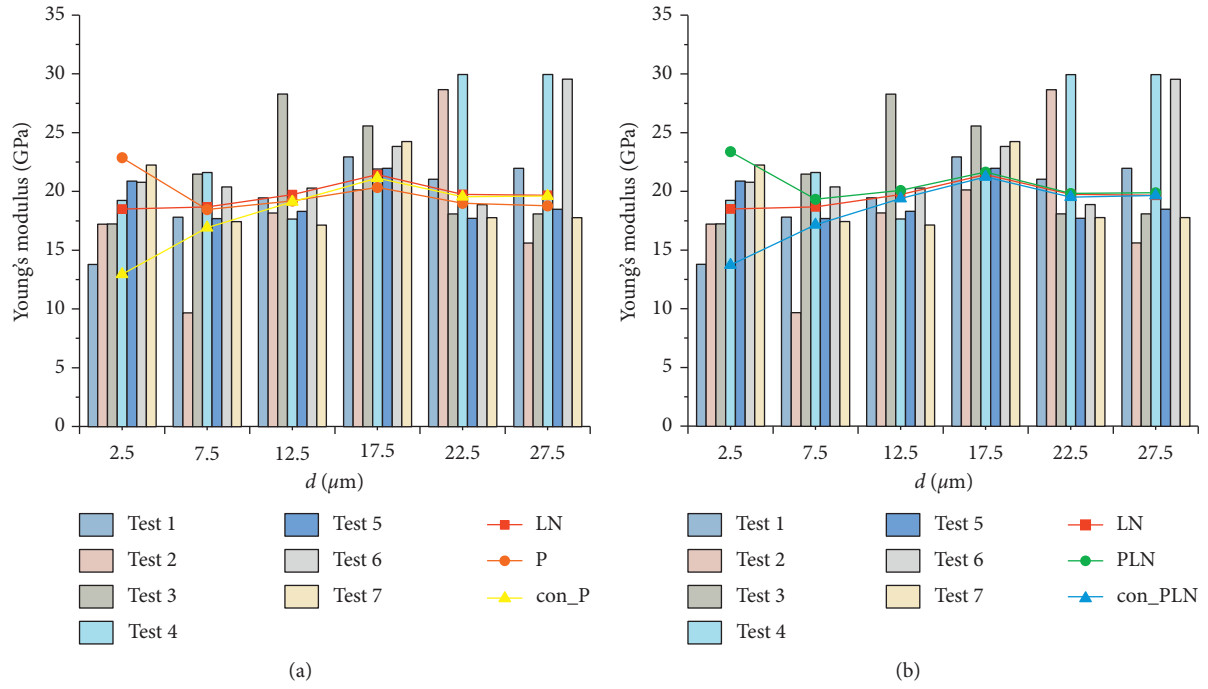

Figure 7: Comparison among all test and calculated results.

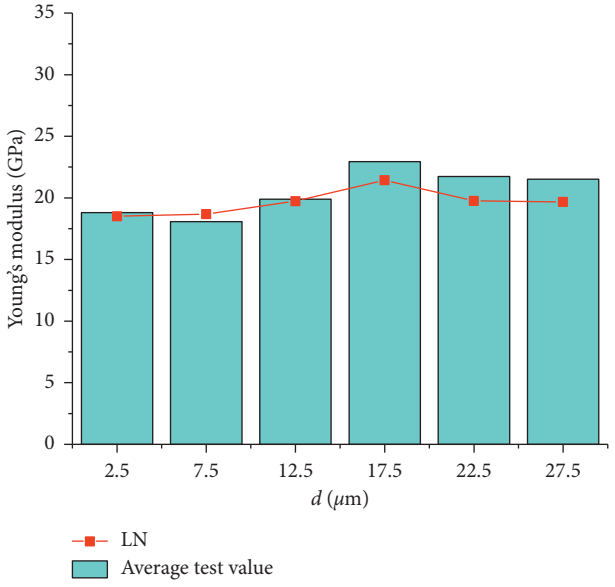

Figure 8: Comparison between test average results and calculated results assuming LN distribution of CH voids.

Table 5: Deviation of average ITZ Young's modulus.

	ITZ					Bulk paste
d (μm)	2.5	7.5	12.5	17.5	22.5	27.5
Average deviation (LN)	−0.088	0.016	−0.009	−0.068	−0.098	−0.087

Table 6: Deviation of upper limit of ITZ Young's modulus.

	ITZ					Bulk paste
d (μm)	2.5	7.5	12.5	17.5	22.5	27.5
Average deviation (con_P)	0.102	−0.152	−0.325	−0.201	−0.372	−0.366
Average deviation (con_PLN)	0.142	−0.091	−0.286	−0.157	−0.340	−0.342

Table 7: Deviation of lower limit of ITZ Young's modulus.

	ITZ				Bulk paste	
d (μm)	2.5	7.5	12.5	17.5	22.5	27.5
Average deviation (con_P)	0.052	0.712	0.081	0.052	0.101	0.248
Average deviation (con_PLN)	0.016	0.774	0.086	0.052	0.105	0.256

Table 8: Components of Eshelby tensor for void inclusion.

	Flat rotating ellipsoidal void ($\alpha < 1$)	Spherical void ($\alpha = 1$)	Prolate rotating ellipsoidal void ($\alpha > 1$)
S_{1111}	$(2-\nu)/(1-\nu)\mathcal{J}_1 + 3A_{11}^{(1)}$	$(7-5\nu)/(15(1-\nu))$	$(2-\nu)/(1-\nu)\mathcal{J}_1 + 3A_{11}^{(1)}$
S_{2222}	$(2-\nu)/(1-\nu)\mathcal{J}_2 + 3A_{22}^{(1)}$	$(7-5\nu)/(15(1-\nu))$	$(2-\nu)/(1-\nu)\mathcal{J}_2 + 3A_{22}^{(1)}$
S_{3333}	$(2-\nu)/(1-\nu)\mathcal{J}_2 + 3A_{22}^{(1)}$	$(7-5\nu)/(15(1-\nu))$	$(2-\nu)/(1-\nu)\mathcal{J}_2 + 3A_{22}^{(1)}$
S_{1122}	$\nu/(1-\nu)\mathcal{J}_1 + A_{12}^{(1)}$	$(5\nu-1)/(15(\nu-1))$	$\nu/(1-\nu)\mathcal{J}_1 + A_{12}^{(1)}$
S_{2211}	$\nu/(1-\nu)\mathcal{J}_2 + A_{12}^{(1)}$	$(5\nu-1)/(15(\nu-1))$	$\nu/(1-\nu)\mathcal{J}_2 + A_{12}^{(1)}$
S_{1133}	$\nu/(1-\nu)\mathcal{J}_1 + A_{12}^{(1)}$	$(5\nu-1)/(15(\nu-1))$	$\nu/(1-\nu)\mathcal{J}_1 + A_{12}^{(1)}$
S_{3311}	$\nu/(1-\nu)\mathcal{J}_2 + A_{12}^{(1)}$	$(5\nu-1)/(15(\nu-1))$	$\nu/(1-\nu)\mathcal{J}_2 + A_{12}^{(1)}$
S_{2233}	$\nu/(1-\nu)\mathcal{J}_2 + A_{22}^{(1)}$	$(5\nu-1)/(15(\nu-1))$	$\nu/(1-\nu)\mathcal{J}_2 + A_{22}^{(1)}$
S_{3322}	$\nu/(1-\nu)\mathcal{J}_2 + A_{22}^{(1)}$	$(5\nu-1)/(15(\nu-1))$	$\nu/(1-\nu)\mathcal{J}_2 + A_{22}^{(1)}$
S_{1212}	$(\mathcal{J}_1+\mathcal{J}_2)/2 + A_{12}^{(1)}$	$(5\nu-4)/(15(\nu-1))$	$(\mathcal{J}_1+\mathcal{J}_2)/2 + A_{12}^{(1)}$
S_{1313}	$(\mathcal{J}_1+\mathcal{J}_2)/2 + A_{12}^{(1)}$	$(5\nu-4)/(15(\nu-1))$	$(\mathcal{J}_1+\mathcal{J}_2)/2 + A_{12}^{(1)}$
S_{2323}	$\mathcal{J}_2 + A_{22}^{(1)}$	$(5\nu-4)/(15(\nu-1))$	$\mathcal{J}_2 + A_{22}^{(1)}$

Table 9: Components for flat rotating ellipsoidal void.

	Flat rotating ellipsoidal void ($\alpha < 1$)
$\mathcal{J}_1$	$\alpha/(1-\alpha^2)^{3/2}(\sqrt{1-\alpha^2}/\alpha - \arccos\alpha)$
$\mathcal{J}_2$	$\alpha/2(1-\alpha^2)^{3/2}(\arccos\alpha - \alpha\sqrt{1-\alpha^2})$
$A_{11}^{(1)}$	$1/(6(1-\nu))[1 + (\alpha^2-3)/(1-\alpha^2)^2 + (\alpha(3\arccos\alpha - \alpha^3\sqrt{1-\alpha^2}))/(1-\alpha^2)^{5/2}]$
$A_{22}^{(1)}$	$1/(16(1-\nu))[2 + ((4\alpha^3-3\alpha)(\arccos\alpha - \alpha\sqrt{1-\alpha^2}) + 2(\alpha^2-1)\sqrt{1-\alpha^2})/(1-\alpha^2)^{5/2}]$
$A_{12}^{(1)}$	$1/4(1-\nu)(1-\alpha^2)^{5/2}[3\alpha^2\sqrt{1-\alpha^2} - (2\alpha^3+\alpha)\arccos\alpha]$

when con_P or con_PLN distribution, and the average value when LN distribution. The estimation on upper and lower limit is conservative relatively, while that on average value showed small deviation. Considering the discreteness of test results themselves, there is no sense to analyse the discreteness of calculated results. Deviations about all the estimation are shown in Tables 5–7.

5. Conclusion

A macro Young's modulus calculation model of ITZ was proposed in this paper. With the introduction of void shape parameter and calcium hydroxide enrichment parameter, and the combination of local water-cement ratio, aggregate volume fraction, and local porosity, Young's modulus of ITZ could be obtained.

This model, with an advantage of small computation, could cover the upper and lower limit and average value of Young's modulus of ITZ and reflect the gradient variation along direction perpendicular to aggregate surface. The availability of the model when $w = 0.5$ was verified through comparison with test results in a reference paper.

For the sake of limited research scope of gravel-cement paste transition zone and limited test data for verification, the proposed model was mainly adopted to ITZ in natural aggregate concrete at present. In addition, this suggested model could provide both theoretical support for meticulous modeling and failure analysis on concrete, and theoretical tool for improvement of ITZ properties in concrete strength research.

The suggested formula of calcium hydroxide enrichment parameter was empirical, while the coupling effect of water enrichment and ion migration was the basic cause of calcium hydroxide enrichment. This coupling effect would be the theme of further study.

Appendix

A. Eshelby Tensor Corresponding to Different Void Inclusion Shape

Remark: the expressions were derived from [31], unwritten components were calculated according to Voigt symmetry,

Table 10: Components for prolate rotating ellipsoidal void.

	Prolate rotating ellipsoidal void ($\alpha > 1$)
$\mathcal{J}_1$	$\alpha/(\alpha^2-1)^{3/2}[\ln(\alpha+\sqrt{\alpha^2-1})-\sqrt{\alpha^2-1}/\alpha]$
$\mathcal{J}_2$	$\alpha/2(\alpha^2-1)^{3/2}[\ln(\alpha-\sqrt{\alpha^2-1})+\alpha\sqrt{\alpha^2-1}]$
$A_{11}^{(1)}$	$1/6(1-\nu)[1+(3\alpha\ln(\alpha+\sqrt{\alpha^2-1})-(\alpha^4-\alpha^2+3)\sqrt{\alpha^2-1})/((\alpha^2-1)^{5/2})]$
$A_{22}^{(1)}$	$1/16(1-\nu)[2+((\alpha-4\alpha^3)[\ln(\alpha-\sqrt{\alpha^2-1})+\alpha\sqrt{\alpha^2-1}]+2(\alpha^2-1)\sqrt{\alpha^2-1})/((\alpha^2-1)^{5/2})]$
$A_{12}^{(1)}$	$1/(4(1-\nu)(\alpha^2-1)^{5/2})[\alpha\ln(\alpha-\sqrt{\alpha^2-1})+3\alpha^2\sqrt{\alpha^2-1}-2\alpha^3\ln(\alpha+\sqrt{\alpha^2-1})]$

and those inconsistent with Voigt symmetry were 0 (Tables 8–10).

B. Distribution Parameter Values Corresponding to Different Porosity (Tables 11–15)

Table 11: Parameter values for LN distribution.

d (μm)	φ^{re} (%)	α_{cr}	σ
2.5	50.00	1.023	0.015
7.5	33.89	1.243	0.141
12.5	22.88	1.512	0.268
17.5	13.96	1.936	0.428
22.5	10.00	2.288	0.536
27.5	10.00	2.288	0.536

Table 12: Parameter values for P distribution.

d (μm)	φ^{re} (%)	α_{cr}	θ	β
2.5	50.00	1.023	0.967	101.256
7.5	33.89	1.243	0.722	10.585
12.5	22.88	1.512	0.538	5.569
17.5	13.96	1.936	0.371	3.486
22.5	10.00	2.288	0.289	2.782
27.5	10.00	2.288	0.289	2.782

Table 13: Parameter values for con_P distribution.

d (μm)	φ^{re} (%)	α_{cr}	θ	β
2.5	50.00	1.023	0.967	101.256
7.5	33.89	1.243	0.722	10.585
12.5	22.88	1.512	0.538	5.569
17.5	13.96	1.936	0.371	3.486
22.5	10.00	2.288	0.289	2.782
27.5	10.00	2.288	0.289	2.782

Table 14: Parameter values for PLN distribution.

d (μm)	φ^{re} (%)	α_{cr}	θ	β	σ
2.5	50.00	1.023	0.997	143.193	0.008
7.5	33.89	1.243	1.027	16.165	0.081
12.5	22.88	1.512	1.201	9.535	0.170
17.5	13.96	1.936	2.102	7.999	0.311
22.5	10.00	2.288	0.900	2.302	0.019
27.5	10.00	2.288	0.900	2.302	0.019

Table 15: Parameter values for con_PLN distribution.

d (μm)	φ^{re} (%)	α_{cr}	θ	β	σ
2.5	50.00	1.023	0.978	113.570	0.004
7.5	33.89	1.243	0.811	11.853	0.035
12.5	22.88	1.512	0.660	6.081	0.062
17.5	13.96	1.936	0.501	3.830	0.092
22.5	10.00	2.288	0.412	3.039	0.109
27.5	10.00	2.288	0.412	3.039	0.109

Data Availability

Previously reported ITZ Young's modulus data were used to support this study and are available at https://www.mendeley.com/catalogue/65b2e568-a37e-3f4c-8fbc-677ba0dbc068/. These prior studies (and datasets) are cited at relevant places within the text as references [15].

Conflicts of Interest

The authors declare that they have no conflicts of interest.

Acknowledgments

The authors would like to acknowledge the financial support provided to this study by the National Natural Science Foundation of China (grant no. 51878546), the Innovative Talent Promotion Plan of Shaanxi Province (grant no. 2018KJXX-056), the Key Research and Development Projects of Shaanxi Province (grant no. 2018ZDCXL-SF-03-03-02), the Science and Technology Innovation Base of Shaanxi Province (grant no. 2017KTPT-19), and the Outstanding Youth Science Foundation of Shaanxi Province (grant no.2020JC-46).

References

[1] K. M. Lee and J. H. Park, "A numerical model for elastic modulus of concrete considering interfacial transition zone," *Cement and Concrete Research*, vol. 38, no. 3, pp. 396–402, 2008.

[2] M. P. Lutz, P. J. M. Monteiro, and R. W. Zimmerman, "Inhomogeneous interfacial transition zone model for the bulk modulus of mortar," *Cement and Concrete Research*, vol. 27, no. 7, pp. 1113–1122, 1997.

[3] S. Mindess, "Bonding in cementitious composites: how important is it?" *MRS Online Proceedings Library Archive*,

vol. 114, 1987.

[4] K. L. Scrivener, A. K. Crumbie, and P. Laugesen, "The interfacial transition zone (ITZ) between cement paste and aggregate in concrete," *Interface Science*, vol. 12, no. 4, pp. 411–421, 2004.

[5] P. Simeonov and S. Ahmad, "Effect of transition zone on the elastic behavior of cement-based composites," *Cement and Concrete Research*, vol. 25, no. 1, pp. 165–176, 1995.

[6] K. Z. J. Wu, "The influence of the matrix-aggregate bond on the strength and brittleness of concrete," *MRS Proceedings*, vol. 114, 1987.

[7] X. Q. Zhou and H. Hao, "Mesoscale modelling of concrete tensile failure mechanism at high strain rates," *Computers & Structures*, vol. 86, no. 21-22, pp. 2013–2026, 2008.

[8] A. U. Nilsen and P. J. M. Monteiro, "Concrete: a three phase material," *Cement & Concrete Research*, vol. 23, no. 1, pp. 147–151, 1993.

[9] T. Chun'an, F. Yufang, and Z. ancheng, "Numerical approach to effect of interface properties on failure modes in particle filled composite," *Acta Materiae Compositae Sinica*, vol. 16, pp. 112–120, 1999, in Chinese.

[10] C. Liu, Z. Fan, X. Chen, C. Zhu, H. Wang, and G. Bai, "Experimental study on bond behavior between section steel and RAC under full replacement ratio," *KSCE Journal of Civil Engineering*, vol. 23, no. 3, pp. 1159–1170, 2019.

[11] C. Liu, Z. Lv, C. Zhu, G. Bai, and Y. Zhang, "Study on calculation method of long term deformation of RAC beam based on creep adjustment coefficient," *KSCE Journal of Civil Engineering*, vol. 23, no. 1, pp. 260–267, 2019.

[12] X. H. Zhao and W. F. Chen, "Effective elastic moduli of concrete with interface layer," *Computers & Structures*, vol. 66, no. 2-3, pp. 275–288, 1998.

[13] J. C. Nadeau, "A multiscale model for effective moduli of concrete incorporating ITZ water-cement ratio gradients, aggregate size distributions, and entrapped voids," *Cement and Concrete Research*, vol. 33, no. 1, pp. 103–113, 2003.

[14] R. L. Berger, D. S. Cahn, and J. D. Mcgregor, "Calcium hydroxide as a binder in portland cement paste," *Journal of the American Ceramic Society*, vol. 53, 1970.

[15] P. Mondal, *Nanomechanical properties of cementitious materials*, Ph.D. thesis, Northwestern University, Evanston, IL, USA, 2008.

[16] W. Zhu, "Microstructure and properties of interfacial transition zone in SCC," in *Proceedings of the SCC'2005-China-1st International Symposium on Design, Performance and Use of Self-Consolidating Concrete*, Changsha, China, 2005.

[17] Y. Xie, D. J. Corr, F. Jin, H. Zhou, and S. P. Shah, "Experimental study of the interfacial transition zone (ITZ) of model rock-filled concrete (RFC)," *Cement & Concrete Composites*, vol. 55, pp. 223–231, 2015.

[18] J. Xu, B. Wang, and J. Zuo, "Modification effects of nanosilica on the interfacial transition zone in concrete: a multiscale approach," *Cement & Concrete Composites*, vol. 81, pp. 1–10, 2017.

[19] J. A. Rossignolo, M. S. Rodrigues, M. Frias, S. F. Santos, and H. S. Junior, "Improved interfacial transition zone between aggregate-cementitious matrix by addition sugarcane industrial ash," *Cement & Concrete Composites*, vol. 80, pp. 157–167, 2017.

[20] C. W. Hargis, *Advances in Sustainable Cements*, 2013, https://escholarship.org/uc/item/4n67v8d6.

[21] C. Liu, H. Liu, C. Zhu, and G. Bai, "On the mechanism of internal temperature and humidity response of recycled aggregate concrete based on the recycled aggregate porous interface," *Cement and Concrete Composites*, vol. 103, pp. 22–35, 2019.

[22] B. D. Barnes, S. Diamond, and W. L. Dolch, "The contact zone between portland cement paste and glass "aggregate" surfaces," *Cement and Concrete Research*, vol. 8, no. 2, pp. 233–243, 1978.

[23] D. Sun, H. Shi, K. Wu, S. Miramini, B. Li, and L. Zhang, "Influence of aggregate surface treatment on corrosion resistance of cement composite under chloride attack," *Construction and Building Materials*, vol. 248, Article ID 118636, 2020.

[24] D. Sun, K. Wu, H. Shi, L. Zhang, and L. Zhang, "Effect of interfacial transition zone on the transport of sulfate ions in concrete," *Construction and Building Materials*, vol. 192, pp. 28–37, 2018.

[25] D. Sun, K. Wu, H. Shi, S. Miramini, and L. Zhang, "Deformation behaviour of concrete materials under the sulfate attack," *Construction and Building Materials*, vol. 210, pp. 232–241, 2019.

[26] M. P. Lutz and R. W. Zimmerman, "Effect of the interphase zone on the bulk modulus of a particulate composite," *Journal of Applied Mechanics*, vol. 63, no. 4, pp. 855–861, 1996.

[27] J. C. Nadeau, "Water-cement ratio gradients in mortars and corresponding effective elastic properties," *Cement and Concrete Research*, vol. 32, no. 3, pp. 481–490, 2002.

[28] J. Xiao, W. Li, Z. Sun, D. A. Lange, and S. P. Shah, "Properties of interfacial transition zones in recycled aggregate concrete tested by nanoindentation," *Cement and Concrete Composites*, vol. 37, pp. 276–292, 2013.

[29] A. C. Gray, *Crystal Morphology and Surface Reactivity Studies of Calcium Hydroxide*, Brunel University, Uxbridge, UK, 1990.

[30] Z. Weiling, S. Wei, C. Cuicui, and M. Changwen, "Characterization for micro mechanical properties of cementitious materials by nanoindentation technique," *Journal of Southeast University (Natural Science Edition)*, vol. 41, pp. 160–165, 2011, in Chinese.

[31] X. Jin, D. Lyu, X. Zhang, Q. Zhou, Q. Wang, and L. M. Keer, "Explicit analytical solutions for a complete set of the Eshelby tensors of an ellipsoidal inclusion," *Journal of Applied Mechanics*, vol. 83, no. 12, 2016.

[32] D. G. Raheja and M. Allocco, *Assurance Technologies Principles and Practices: A Product, Process, and System Safety Perspective*, John Wiley & Sons, Hoboken, NJ, USA, 2006.

[33] D. P. M. Scollnik and P. M. David, "On composite lognormal-Pareto models," *Scandinavian Actuarial Journal*, vol. 2007, no. 1, pp. 20–33, 2007.

[34] G. P. Tandon and G. J. Weng, "Average stress in the matrix and effective moduli of randomly oriented composites," *Composites Science and Technology*, vol. 27, no. 2, pp. 111–132, 1986.

[35] Y. Gao, G. De Schutter, G. Ye, Z. Tan, and K. Wu, "The ITZ microstructure, thickness and porosity in blended cementitious composite: effects of curing age, water to binder ratio and aggregate content," *Composites Part B Engineering*, vol. 60, pp. 1–13, 2014.

[36] G. J. Weng, "Some elastic properties of reinforced solids, with special reference to isotropic ones containing spherical inclusions," *International Journal of Engineering Science*, vol. 22, no. 7, pp. 845–856, 1984.